Agricultural and Forest Meteorology 197 (2014) 91–102

Contents lists available at ScienceDirect

Agricultural and Forest Meteorology

journal homepage: www.elsevier.com/locate/agrformet

Using evapotranspiration to assess drought sensitivity on a subfield scale with HRMET, a high resolution surface energy balance model

Samuel C. Zipper[a,*], Steven P. Loheide II[a,b,1]

[a] Freshwater & Marine Sciences Program, University of Wisconsin-Madison, Madison, WI USA
[b] Department of Civil & Environmental Engineering, University of Wisconsin-Madison, Madison, WI USA

ARTICLE INFO

Article history:
Received 24 January 2014
Received in revised form 3 April 2014
Accepted 17 June 2014

Keywords:
Energy balance
Evapotranspiration
Precision agriculture
Drought response
Thermal imagery
Spatial heterogeneity
Yield monitoring

ABSTRACT

Evapotranspiration (ET) rates provide a valuable within-season indicator of plant productivity, as well as data on fluxes of water in a landscape. Applying remote sensing for ET estimation has potential to improve the sustainable management of water resources in agricultural settings. Most current ET models, however, rely on 'dry' and 'wet' pixels within a given scene to partition turbulent fluxes between latent and sensible heat, thus limiting their ability to map ET throughout the growing season at extremely high (meter scale) spatial resolutions. Here, we develop a field-validated surface energy balance model, High Resolution Mapping of EvapoTranspiration (HRMET), which requires only basic meteorological data, spatial surface temperature and canopy structure data. We use HRMET to estimate ET rates over two commercial cornfields in south-central Wisconsin during the 2012 growing season, which was characterized by severe drought. HRMET results indicate that the magnitude of within-field variability in ET rates was primarily driven by water availability. The application of remotely sensed data to precision agriculture has also been hampered by turnaround time between image acquisition and availability. We introduce relative ET (ET_R), which enables comparison of ET rates between image dates by normalizing for variability caused by weather and crop stage. ET_R also provides an intuitive, index-like metric for evaluating spatial variability in ET on a subfield scale. ET_R maps illuminate persistent patterns in ET across measurement dates that may be driven by soil water availability and topography. ET_R is used to develop a novel paired-image technique that can map subfield sensitivity classes to stressors such as drought. Sensitivity class mapping can be used to circumvent issues related to turnaround time to facilitate the incorporation of remotely sensed data into precision agriculture.

Published by Elsevier B.V.

1. Introduction

Spatially distributed estimates of evapotranspiration (ET) are a critical agricultural resource (Gowda et al., 2007). Farmers, agronomists, and water resource managers need accurate data about plant water use to evaluate irrigation requirements, respond to drought or precipitation events, and forecast year-end yields (Hiler et al., 1974; Idso et al., 1977; Kanwar et al., 1984; Akhtar et al., 2013; Kresovic et al., 2013). ET estimates can also enhance ecosystem and agroecosystem models by providing estimates of mass and energy fluxes over the landscape (Kucharik and Brye, 2003; Kucharik and Twine, 2007; Soylu et al., 2014).

Spatially distributed estimates of ET are particularly useful for applications in precision agriculture, for which high spatial resolution is a necessity. The fundamental theory behind precision agriculture is that the optimum inputs vary spatially on the subfield scale, depending on factors such as soil texture, soil organic matter, water availability, topography, and more (Wibawa et al., 1993; Kravchenko and Bullock, 2000; Schmidt et al., 2002; Kravchenko et al., 2003; Schepers et al., 2004). Many techniques have been used to estimate spatially distributed ET rates from both agricultural and natural settings using remotely sensed data. Glenn et al. (2007), Gowda et al. (2007) and Maes and Steppe (2012) provide reviews of the techniques available. One class of ET models are surface energy balance models, which attempt to estimate the partitioning of available energy (A) at the land surface to determine the relative magnitudes of the sensible heat flux (H) and latent heat flux

* Corresponding author. Department of Civil & Environmental Engineering, University of Wisconsin-Madison, 1415 Engineering Dr, Room 1226, Madison WI 53706 USA. Tel.: +1 206 909 1277.
E-mail addresses: szipper@wisc.edu, samuelczipper@gmail.com (S.C. Zipper), loheide@cae.wisc.edu (S.P. Loheide II).
[1] Department of Civil and Environmental Engineering, University of Wisconsin-Madison, 1415 Engineering Drive, 1269C Engineering Hall, Madison, WI 53706, USA. Tel.: +1 608 265 5277.

http://dx.doi.org/10.1016/j.agrformet.2014.06.009
0168-1923/Published by Elsevier B.V.

(λET), which is directly related to the ET rate. The general surface energy balance equation is as follows:

$$R - G = A = H + \lambda ET \quad (1)$$

where R is equal to net incoming radiation, G is the heat flux into the subsurface, and all units are in [W m^{-2}].

Surface energy balance models relying on remotely sensed data typically require surface reflectance data in one or more wavelengths and surface temperature data, all of which are available on common sensor platforms. Commonly used models include SEBAL (Bastiaanssen et al., 1998), METRIC (Allen et al., 2007), and SEBI (Menenti and Choudhury, 1993; Roerink et al., 2000). These models rely on the presence of a 'dry' (also referred to as 'hot') and 'wet' ('cool') pixel within the image to define the extremes of surface temperature, where all available energy is apportioned to sensible heat or latent heat fluxes, respectively. Other energy balance models, such as ALARM (Suleiman & Crago, 2004), have been shown to work in the absence of dry and wet pixels, but assume a closed canopy to simplify canopy transport physics. Previous energy balance models have been applied effectively over large areas (Elhaddad et al., 2010; Bastiaanssen et al., 2012) and small spatial scales with diverse land surface cover (Loheide and Gorelick, 2005).

However, these widely used energy balance techniques are typically applied at regional scales using moderate spatial resolution (30–1000 m) satellite data, and are structurally incompatible with high-resolution remote sensing of crops. Though field-scale management based on ET estimates have been practiced with some success (Folhes et al., 2009; Ko and Piccinni, 2009; M. C. Anderson et al., 2012a; R. G. Anderson et al., 2012b), subfield-scale precision management based on remotely sensed ET estimates has not yet been attempted. Many agricultural landscapes are fairly homogeneous, making it difficult or impossible to identify dry and wet pixels within the same image–for high resolution image collection required for precision agricultural management, image extent can be limited to $\leq$1 km^2. For most agricultural settings, completely closed canopies are rarely available during the early growing season, and dry or fallow open canopies are rarely available late in the growing season, limiting these models' application to transient dynamics in ET. Furthermore, while satellite-based estimates of ET are useful for landscape scale studies, even the highest-resolution multispectral and thermal satellites are insufficiently detailed for most subfield scale applications.

To address these issues unique to ET estimation at small spatial scales with homogeneous canopies, we developed a mixed-input surface energy balance model for the High Resolution Mapping of EvapoTranspiration (HRMET). HRMET employs high-resolution ($\sim$1–2.5 m) surface temperature data collected at a subfield scale in conjunction with 30 m resolution Landsat imagery and local meteorological data to estimate the surface energy balance. HRMET uses a combination of physical and empirical relationships to calculate A, and an iterative approach to calculate H which does not require wet and dry pixels. λET is estimated as the residual and converted to an instantaneous ET rate. A full model description is found in Section 3.

While spatially distributed estimates of ET are an essential tool for hydrologists and water resource managers (M. C. Anderson et al., 2012a), a major limitation of applying ET mapping to agricultural management at all scales is the difficulty in making comparisons between image collection dates. A "good" ET rate can vary widely between dates due both to stress-related changes (e.g. stomatal closure caused by drought) and changes out of a farmer's control (e.g. crop growth stage, weather conditions). This makes management based on ET data from different measurement dates challenging and non-intuitive.

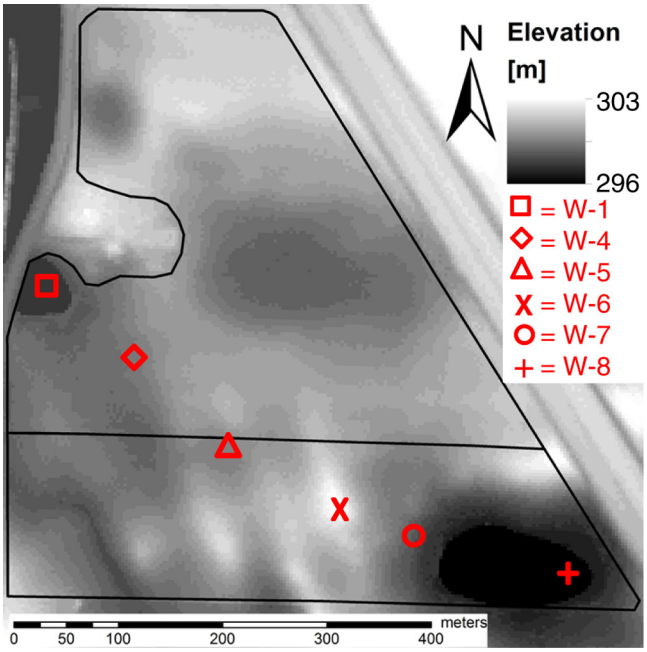

Fig. 1. Northern and southern fields overlain onto DEM of study site. Red shapes correspond to field measurement sites of LAI and canopy height.

For this reason, most remotely sensed analyses of crop drought response use stress indices such as the crop water stress index (CWSI; Jackson et al., 1981), water deficit index (Moran et al., 1994), perpendicular drought index (Shahabfar and Eitzinger, 2011), or the integrated surface drought index (Wu et al., 2013). The primary advantage of these indices is a low data requirement and intuitive interpretation; the CWSI, for example, ranges from 0 to 1. To bridge this gap between the utility of physically-based ET estimates valued by hydrologists and intuitive stress indices valued by land managers, we introduce relative ET (ET_R). ET_R is a novel way to interpret HRMET's spatially distributed ET estimates and allows us to easily compare measurement dates in the manner of a crop stress index. We compare corn response to a severe drought during the 2012 growing season, using a study site in south-central Wisconsin as an exemplar. ET_R allows us to identify persistent patterns of ET on a subfield scale, which could be used to target areas of the field for precision management such as variable rate water application during drought (King and Kincaid, 2004). We also demonstrate how deviations from these patterns can be used to identify drought-sensitive and moisture-sensitive areas on a subfield scale. Identification of these stress-sensitive areas can guide precision management decisions, even in the absence of real-time remotely sensed data.

2. Study site

Our study site is two adjacent commerically-managed corn fields in south-central Wisconsin. Fig. 1 shows the study site, separated into a northern field (12 ha) and a southern field (9 ha), with six transect points noted. Soil classes throughout the study site are predominantly silt loams and silty clay loams, with 3–6% organic matter by mass in the top 0.1 m. Topsoils extend to a depth of $\geq$0.5 m at all transect points. There is approximately 7 m of topographic relief across the site, with steeper terrain in the southern field and gradual slopes in the northern field. Figure 1 shows three elongate hills, extending from the southern edge of the field to the north-northwest; these are small glacial moraines, and have a coarser soil texture (loam to silt loam) and lower organic content (1–3%) than surrounding soils (Clayton and Attig, 1997).

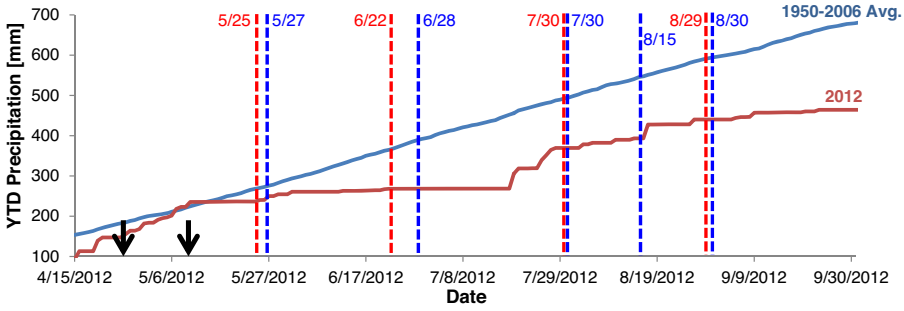

Fig. 2. Cumulative precipitation over the 2012 growing season with imagery collection dates overlaid. Red lines correspond to surface temperature measurements and blue correspond to cloud-free Landsat scenes. Black arrows show planting date of the northern (4/26/2012) and southern fields (5/10/2012).

Management is consistent between the two fields, with the exception of planting date (Fig. 2) and harvesting; in 2012, the northern field was planted on April 26 [Day Of Year (DOY) 117] and harvested for silage on September 5 (DOY 249), and the southern field was planted on May 10 (DOY 131) and harvested for grain on October 25 (DOY 299). Both fields were planted at a density of 13,760 plants/ha. The fields have been in a corn/hay rotation since the 1970s, with predominantly corn planted in the preceding two decades, including the 2010 and 2011 growing seasons. Both fields also received the same nutrient input. Prior to planting, manure equivalent to 108 kg N/ha and 81 kg P/ha was spread over both fields on March 16 (DOY 76). 37 kg/ha of 28% N fertilizer was applied during planting and an additional 64 kg/ha in early June.

3. Model structure

HRMET is a mechanistic model intended to estimate the relative magnitude of the constituents of the energy balance at the land surface. It relies on three primary inputs: basic meteorological data, remotely sensed land surface temperature, and a remotely sensed model of canopy characteristics (Fig. 3). Here, we present the physical and empirical relationships underlying HRMET.

3.1. HRMET theory

HRMET is a pixel-based model that uses a combination of physical principles and established empirical relationships to calculate ET as the residual of the land surface energy balance (Eq. (1)). Pixel size is determined using the spatial resolution of surface temperature data. We assume there is no lateral communication between pixels. At each pixel, available energy is calculated using equations that account for spatially variable canopy radiation interception characteristics (see Section 3.3). H is calculated using the gradient between the surface temperature (T; °C) and the air temperature some distance above the canopy (T_{air}; °C):

$$H = \frac{\rho_a c_p (T - T_{air})}{r_{Ha} + r_{ex}} \quad (2)$$

where ρ_a and c_p are the molar density [mol m^{-3}] and specific heat [J mol^{-1} C^{-1}]of air, respectively, and the denominator includes the aerodynamic resistance to heat transport (r_{Ha}; s m^{-1}) and the excess resistance to heat transport (r_{ex}; s m^{-1}). A detailed approach to solving Eq. (2) is presented in Section 3.4. Using r_{ex} allows us to ignore the difference between the aerodynamic and surface temperatures (Norman and Becker, 1995). H and r_{Ha} are co-dependent, as the magnitude of H influences atmospheric stability and thus the resistance to heat transport; therefore, HRMET uses an iterative approach following Bastiaanssen et al. (1998) to converge on a final solution for H and λET.

We use HRMET with a novel permutation-based approach for calculating the land surface energy balance which allows us to incorporate the uncertainty inherent in the input variables into final results, based on Serbin et al. (2014). HRMET is solved 100 times at each point. For each permutation, inputs are varied by selecting randomly from a standard normal distribution based on an input mean and standard deviation for each variable (for the uncertainty estimation of each input variable, see Section 3.2). This produces 100 ET estimates at each point using unique input parameters. These are then used to calculate a final mean and standard deviation of estimated ET for each pixel.

3.2. Required inputs

HRMET requires 15 unique inputs, divisible into four categories (Fig. 3).

3.2.1. Inputs- descriptors

Site-specific information includes date & time of the imagery collection and the longitude and latitude of the study site in decimal degrees. These inputs are assumed to have no uncertainty.

3.2.2. Inputs- meteorology

Required meteorological inputs are air temperature (T_{air}; °C), incoming shortwave radiation (SW_{in}; W m^{-2}), wind speed (u; m s^{-1}), air vapor pressure (e_a; kPa), and atmospheric pressure (p_a; kPa). Meteorological inputs were collected at the University of Wisconsin-Madison Arlington Agricultural Research Station (43.31°N, -89.38°W), which is ~2.75 km NE of the study site and collects data every half-hour.

Uncertainty in meteorological inputs was estimated using data collected between one hour before and one hour after image collection. For inputs with a strong time-dependence (T_{air}, SW_{in}), we applied a linear regression to the timeseries and estimated uncertainty as the standard deviation of the residuals from this trend. For inputs with a weak or absent time-dependence (u, e_a, p_a), uncertainty was estimated as the standard deviation of the measurements over the entire interval. Potential spatial variability in meteorological inputs over the limited spatial extent of the site was not incorporated into estimates of uncertainty.

3.2.3. Inputs- surface characteristics

To calculate the land surface radiation balance, both emissivity (ε) and albedo (ρ) are required. We estimated values of ε and ρ separately for the soil and corn surface based on a literature review. Albedos for corn and soil were estimated as 0.2 and 0.105, respectively, with a standard deviation of 0.05. The range of typical ε of natural materials is much smaller than that of ρ. We used 0.94 and 0.945 for the emissivity of corn and soil, respectively, with a standard deviation of 0.01 (Campbell and Norman, 2000; Jury and Horton, 2004).

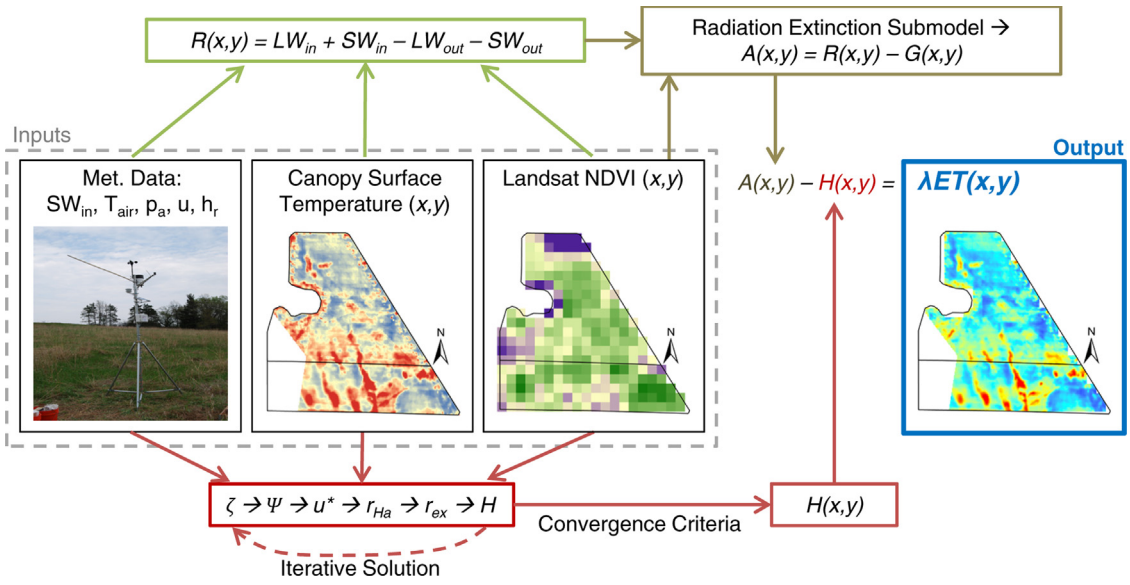

Fig. 3. Conceptual diagram of the required model inputs for the energy balance model and interactions between necessary inputs. Each component of the energy balance requires the same inputs (see Section 3.2 of text), and the model solves for λET.

3.2.4. Inputs- spatially variable

HRMET requires three spatially variable inputs: surface temperature (T), leaf area index (LAI), and canopy height (h). These were estimated using remotely sensed data.

3.2.4.1. Surface temperature. Surface temperature data were collected using a Cessna-mounted FLIR A320 thermal infrared imaging camera (FLIR Systems, Wilsonville, OR, USA) on 4 dates during the 2012 growing season (Fig. 2): May 25 (DOY 145; hereafter referred to as May image), June 22 (DOY 173; June or drought image), July 30 (DOY 211; July or wet image), and August 29 (DOY 241; August image). Flights were all taken in late morning, within 45 min of approximate local Landsat overpass time (11:30 AM CST). Imagery was collected from a height of 900 m above ground surface for the May 25 image, and 1200 m for the other measurement dates, for a pixel size of ~1–2.5 m. Images were atmospherically corrected using ThermaCAM Researcher Pro 2.7 software (FLIR Systems, 2003) and georeferenced to NAIP imagery (National Agricultural Imaging Program, 2010), then mosaicked in ArcMap 10 (ESRI, 2011). Uncertainty in T at each pixel was estimated as the standard deviation of T within a 25-pixel moving window.

3.2.4.2. Canopy characteristics. Vegetation Indices (VIs) from remotely sensed data, such as the normalized difference vegetation index (NDVI), have been used to estimate LAI in many studies (Chen and Cihlar, 1996; Bastiaanssen et al., 1998; Glenn et al., 2007; Zheng and Moskal, 2009). Here, we locally regressed NDVI to estimate LAI and h. Field measurements of LAI and h were collected at 6 transect points within the study site every 5-11 days throughout the 2012 growing season (Fig. 1). LAI measurements were taken using an LAI-2200 Plant Canopy Analyzer (Welles and Norman, 1991; LI-COR, Lincoln NE, USA). Sites were selected to be along a range of soil and moisture conditions, and include points in both the northern and southern fields.

Cloud-free Landsat 7 ETM+ data were retrieved for 5 dates during the 2012 growing season (Figure 2) and atmospherically corrected using the LEDAPS algorithm (Masek et al., 2006). Landsat surface reflectance data was then used to calculate NDVI as

$$NDVI = \frac{NIR - RED}{NIR + RED} \quad (3)$$

where NIR and RED are the reflectance in the near-infrared (0.77–0.9 μm) and red (0.63–0.69 μm) wavelengths. Landsat NDVI values were regressed to LAI and h field measurements using a power model (Fig. 4). Where measurement and imagery dates did not coincide, LAI and h measurements were linearly interpolated between dates. Both regressions yielded strong fits ($R^2 > 0.9$) and showed some saturation at full canopy cover.

We used a permutation-based approach to estimate uncertainty in our regression results for both LAI and h. For each of 100 permutations, 5 random data points were eliminated and a power model regression was fit to the remaining points. The eliminated points were then used to determine the fit of each model. Average root mean squared error (RMSE) was RMSE = 0.91 m^2 m^{-2} for LAI and RMSE = 0.44 m for h. These 100 separate power models were then used to calculate LAI and h from Landsat input data and generate a mean and standard deviation of both canopy characteristics for each pixel.

3.3. Calculation of available energy

R is calculated as the sum of incoming and outgoing (subscript *in* and *out*, respectively) longwave and shortwave radiation (*LW* and *SW*, respectively) where a positive flux means towards the land surface:

$$R = SW_{in} - SW_{out} + LW_{in} - LW_{out} \quad (4)$$

All terms have units of [W m^{-2}].

SW_{in} is measured at a weather station ~2.75 km from the study site, as described in Section 3.2.2. Available energy is calculated using a two-source model, with the soil and canopy surface treated separately (Norman et al., 1995; Chavez et al., 2009). SW_{in} is partitioned between the soil and canopy surface using the radiation extinction model presented in (Norman et al., 1995), which converts LAI to fractional cover and estimates total radiation passing through the canopy. SW_{out} is then calculated separately for the soil and corn canopy surface as ρSW_{in}, where ρ [-] is the albedo for each surface.

LW_{in} and LW_{out} are calculated for the land surface and atmosphere using the Stefan-Boltzmann Law for a graybody:

$$LW = \varepsilon \sigma T^4 \quad (5)$$

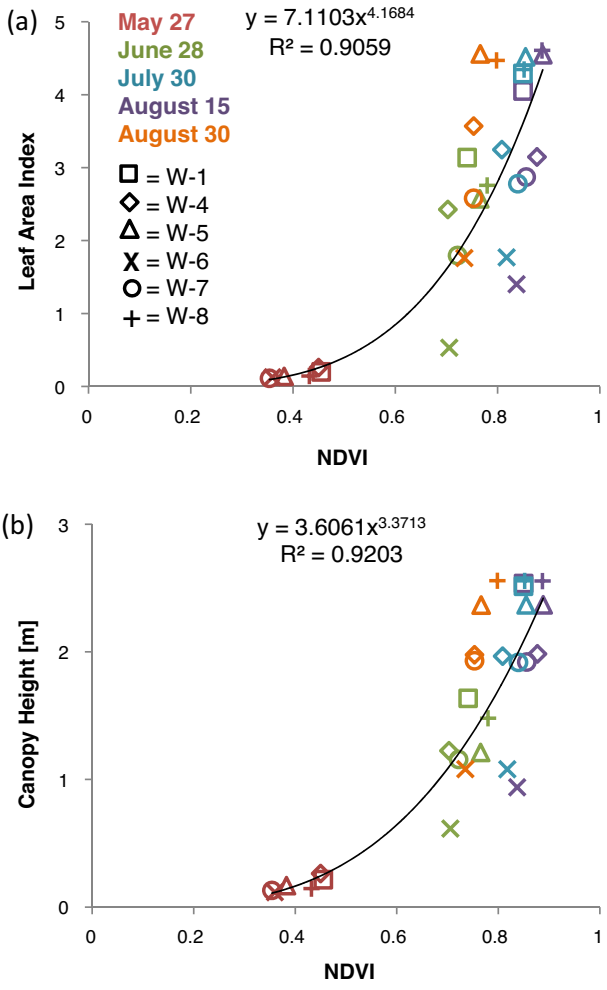

Fig. 4. Regressions of NDVI to (a) LAI and (b) canopy height data from the 2012 growing season ($n = 29$). Any estimates outside the range of observed values ($0\ m \le h \le 3\ m, 0 \le LAI \le 5$) were set to the appropriate limit to avoid overextrapolation. Points are color-coded by date and shape-coded by site, as in Fig. 1.

where ε is the emissivity of the surface [-], σ is the Stefann-Boltzmann constant [W m^{-2} K^{-4}], and T is the temperature of the surface [K]. LW_{in} is calculated using the surface properties of the atmosphere, with a cloudiness-dependent ε calculated based on the difference between observed SW_{in} and expected clear-sky irradiance, following Crawford and Duchon (1999). LW_{out} is calculated using the surface properties of the land surface. G is then calculated as 35% of the energy reaching the ground using the canopy radiation extinction model described above (Norman et al., 1995).

3.4. Iterative calculation of the sensible heat flux

HRMET uses an iterative procedure to converge on the sensible heat flux for each pixel using the following steps:

1. Calculate zero-plane displacement height (d; m), roughness length for momentum transfer (z_{0M}; m), roughness length for heat transfer (z_{0H}; m) as a function of LAI and h, following Raupach (1994).
2. Set arbitrary initial values for H and boundary layer stability factor (ζ) where ζ and H are positive. $\zeta > 0$ indicates unstable boundary layer conditions where buoyant air is rising from the surface.
3. Calculate diabatic correction factor for momentum and heat flux (Ψ_M, Ψ_H) based on ζ, where (Campbell and Norman, 2000):

$$\Psi_M = 6\log(1+\zeta);\ \Psi_H + \Psi_M \text{ when } \zeta < 0. \quad (6)$$

$$\Psi_M = -2\log(1+(1-16\zeta))^{0.5};\ \Psi_H + 0.6\Psi_M \text{ when } \zeta > 0. \quad (7)$$

4. Calculate friction velocity (u*; m s^{-1}; Norman and Becker, 1995)

$$u^* = \frac{uk}{\log\left(\frac{z_u - d}{z_{0M}}\right) + \Psi_M} \quad (8)$$

where z_u is the height of wind speed measurements.

5. Calculate r_{Ha} (Campbell and Norman, 2000):

$$r_{Ha} = \frac{\left(\log\left(\frac{z_u - d}{z_{0M}}\right) + \Psi_M\right)\left(\log\left(\frac{z_T - d}{z_{0H}}\right) + \Psi_H\right)}{k^2 \rho_a u} \quad (9)$$

where z_T is the height of air temperature measurements [m] and k is von Karman's constant [-].

6. Calculate r_{ex} (Norman and Becker, 1995):

$$r_{ex} = \frac{\log\left(\frac{z_{0M}}{z_{0H}}\right)}{\rho_a k u^*} \quad (10)$$

7. Calculate new value of H using Eq. (2).
8. Calculate a new value of ζ (Campbell and Norman, 2000):

$$\zeta = \frac{-9.8 k z_u H}{\rho_a c_p T_{air,K} (u^*)^3} \quad (11)$$

where $T_{air,K}$ is T_{air} in °K.

9. Repeat steps 3–8 until the convergence criteria (≤0.1% change between iterations) is met. At our study site, this typically takes ~10–20 iterations.

Steps 2–9 were then repeated using negative starting values for ζ and H, indicating stable boundary layer conditions. HRMET was considered to have converged on a global solution to H if values from both positive and negative sets of initial conditions are within 0.1% of each other; convergence was achieved at all points in our simulations. This converged H is then used in Eq. (1) to solve for λET.

3.5. Model validation

HRMET was validated by comparison with the Shuttleworth-Wallace (SHW) model (Shuttleworth and Wallace, 1985; Brisson et al., 1998; Zhou et al., 2006). In structure and theory, SHW is very similar to the Penman-Monteith Equation (Monteith, 1965; Allen et al., 1998). SHW was selected for our application because it takes into account evaporation directly from the soil surface during sparse canopy conditions, which includes our May 25 imagery collected shortly after planting.

In addition to the A term calculated for HRMET, SHW requires soil surface resistance and canopy surface resistance terms as inputs. We collected 5 stomatal resistance measurements using a Decagon SC-1 Leaf Diffusion Porometer and 5 soil moisture measurements using a Delta-T ML2x Thetaprobe at each of the 6 transect sites (Fig. 1) on either the day before or the day after the image collection at a similar time of day. Meteorological input variables were analyzed to ensure that conditions were similar between image collection and field measurements.

Estimating soil surface resistance for the bare-soil evaporation term of SHW is done using empirical relationships fit to soil moisture data (Camillo and Gurney, 1986; Kondo et al., 1990; Farahani and Bausch, 1995). We follow the approach of Camillo and Gurney (1986) assuming a spatially uniform saturated soil water content of 0.45 m^3 m^{-3}. To determine canopy surface resistance, we first

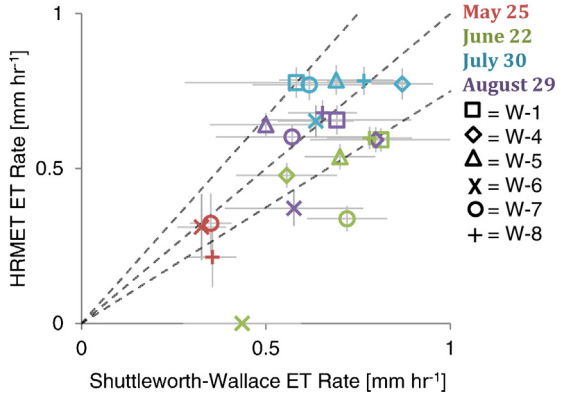

Fig. 5. Comparison of HRMET and Shuttleworth-Wallace estimated ET rate for each all modeled dates. Dashed lines show a 1:1 fit and 25% error in either direction. Error bars represent 1 standard deviation for each model.

calculate the total sunlit LAI using a sunlight extinction model presented in Campbell and Norman (2000) which considers the solar zenith angle, total LAI, and canopy leaf angle distribution. Bulk canopy resistance was then calculated assuming a big-leaf model for only sunlit LAI.

4. Results and discussion

4.1. Model validation

HRMET compared favorably with the SHW validation (Fig. 5). The RMSE of all points was 0.17 mm h^{-1} and all points except two had a percent squared error of ≤12%. Significant leaf-to-leaf variability was observed in stomatal conductance measurements, contributing to a large range of SHW values during the permutation-based analysis. HRMET accurately estimates ET rates during sparse canopy conditions (May image RMSE = 0.08 mm h^{-1}) without any further calibration, indicating that the parameterization of the bare soil resistance was reasonable (Camillo and Gurney, 1986; Chavez et al., 2009).

The largest differences between HRMET and SHW occcur during the June drought image, particularly at sites W-6 and W-7, where HRMET estimates are significantly higher than SHW's. These two sites have the coarsest soil texture and the highest elevation, and thus are sites where we expect the impacts of water stress to appear first (Delin et al., 2000; Kravchenko and Bullock, 2000; Huang et al., 2008). In the field, these sites exhibited reductions in LAI and significant visible wilting, indicating that the sunlit big leaf model used in the SHW technique may be an overestimation of the transpiring LAI during stressed periods.

4.2. Sensitivity analysis

Using HRMET with the permutation-based technique described above takes into account estimated uncertainties for all variables simultaneously to generate estimates of both ET and uncertainty for each pixel. Fig. 6 shows the mean ET rate and Fig. 7 shows uncertainty (expressed as a standard deviation of ET estimates) on a pixel-by-pixel basis from 100 permutations. Uncertainty expressed as a percentage of mean ET is ~30-50% of total ET in the May image (when ET rates are relatively low) and 5–15% of mean ET in the other three images, with the highest spatial variability in uncertainty observed in the June image.

Typically, higher uncertainty is shown in the areas around regions of very low ET (e.g. W-6 in Fig. 7b). This is primarily because of 'hot spots' in the T data; where canopy temperatures are very high, ET rates are very low because of the strong sensible heat flux from the land surface to the atmosphere. Pixels around the edges of these hot spots exhibit a large uncertainty in ET rates because of the spatial variability of T within HRMET's moving window. This phenomenon is also what drives the largest amount of spatial variability during the June image, which is captured during the drought and has the largest range of measured surface temperature data (Gonzalez-Dugo et al., 2006).

Fig. 7 shows the aggregate uncertainty of all variables simultaneously; however, HRMET's sensitivity was also tested to each input variable individually. The largest observed sensitivity was to surface temperature estimates. The observed uncertainty in ET rates due to changes in T estimates was 10^{-2} mm h^{-1} for most pixels, but areas around the hot spots had higher uncertainties in ET, up to 10^{-1} mm h^{-1}. The uncertainty in estimated ET rates as a result of meteorological input data ranged from 10^{-2}–10^{-4} mm h^{-1}, indicating that the assumption of spatially uniform meteorological conditions on a site scale is acceptable (Loheide and Gorelick, 2005). Sensitivity to meteorological data was greatest in May, when the canopy was very sparse and bare-soil evaporation played a larger role.

Uncertainty in ET due to LAI and h estimates was ~10^{-3} mm h^{-1} across all image dates, and sensitivity was inversely correlated with both LAI and h. This indicates that LAI and h estimation errors at full canopy cover due to saturation of NDVI (e.g. M. C. Anderson et al., 2004) is not a significant source of uncertainty for HRMET. There were some apparent edge effects due to the coarser spatial resolution of the Landsat data (e.g. Fig. 6a). These were especially apparent when the canopy was sparse, likely due to overestimation of canopy height due to within-pixel mixing with vegetation around the field edge.

4.3. Magnitude of ET variability

The magnitude of spatial variability in ET rates over the field differs noticeably between dates (Fig. 6). The May image shows strong edge effects, likely due to within-pixel mixing of edge vegetation with the nearly bare soil within field boundaries. Due to the very sparse canopy in the May image (LAI values < 0.5 across both fields), we will exclude the May image from further analysis of ET dynamics.

When all images are plotted on an identical color scale covering the minimum and maximum observed ET rates across all measurement dates, differences in the magnitude of transpiration rate variability over the entire field appears to correspond to field scale water availability on the image date (Gonzalez-Dugo et al., 2006; Berni et al., 2009; Alchanatis et al., 2010). In the June image, where there was only 6.4 mm of recorded precipitation rain in the preceding two weeks, ET rates vary from ~0 to 0.7 mm h^{-1} (Fig. 6b). The range of ET estimates is much smaller during the July and August images (Figure 6c-d), where there was significantly more rainfall (101.1 mm and 47.0 mm, respectively) in the weeks prior to image collection and the majority of the canopy is transpiring at a near-maximum rate of ~0.7–0.8 mm h^{-1}. Slight decreases in ET rates are still visible along the small moraines extending from the south edge of the field, but even these are very close in magnitude to the rest of the field.

Table 1 shows two proxies for water availability (precipitation in the preceding two weeks and mean soil moisture values) on the subfield scale across both measurement dates, for all sites. The variability between dates indicates that the magnitude of ET variability is governed by transient stressors, such as soil water availability (Raghuwanshi and Wallender, 1997). This supports previous research demonstrating larger within-field yield variability during dry years (Lark et al., 1998). Previous studies have suggested that remote sensing may be a valuable tool for irrigation scheduling (Hunsaker et al., 2005; Er-Raki et al., 2007) or drainage

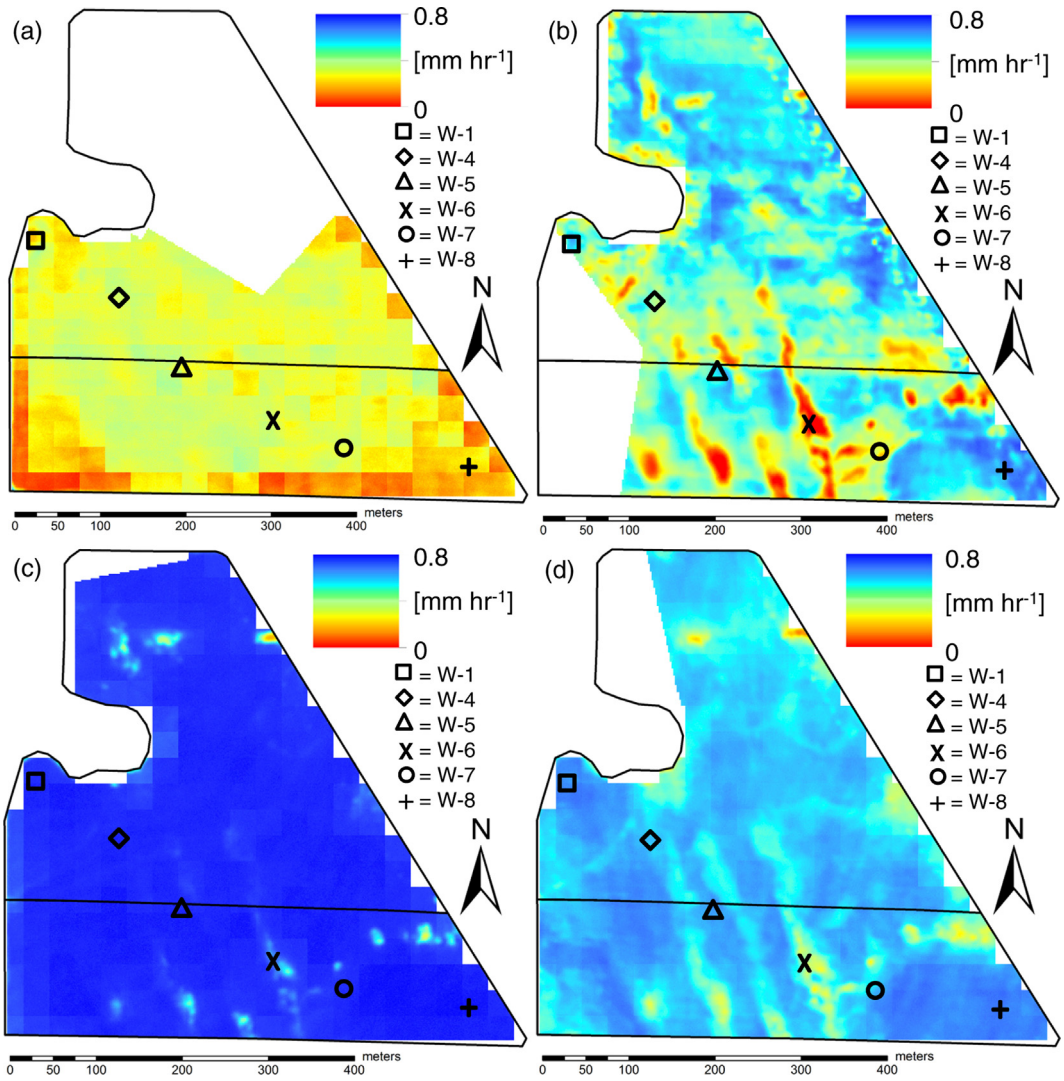

Fig. 6. HRMET-calculated mean ET rates for (a) May 25, (b) June 22, (c) July 30, and (d) August 29 in mm h^{-1}. All images are stretched linearly to the same range. ET rates are calculated as the mean of 100 permutations randomly selecting from within a predefined range of variability for each input (see Section 3 of text for full description). Note that the dominant patterns of spatial variability, visible in the June image, are no longer visible in the post-drought (July and August) images.

water management (Cicek et al., 2010). The correlation between water availability and the magnitude of ET variability on a sub-field scale indicates that HRMET is a valuable tool for identifying water-stressed parts of a field in near-real-time.

4.4. Persistent patterns of ET

While the magnitude of ET variability within the field differs greatly between dates (Fig. 6), there are consistently low-ET portions of the field across all images. To examine persistent spatial trends between dates, we introduce the concept of relative ET (ET_R), defined as absolute ET rates linearly normalized to the 5th and 95th percentile of measured ET rates for a given image (Fig. 8). Therefore, an ET_R of 1 corresponds to the highest ET rates (95th percentile and higher) within a field on a particular date, while an ET_R of 0 is the lowest ET rates (5th percentile and lower) within a field. ET_R allows ET rates to be understood on the same intuitive numeric range as a stress index like the CWSI (Jackson et al., 1981) while retaining a strong physical basis. ET_R also provides a useful tool for comparison of ET across dates, which allows us to study spatially variable responses to field scale external forcings (e.g. weather) or comparisons between crops at different developmental stages.

Using ET_R, persistent patterning is apparent between measurement dates. The coarse-textured, relatively high-elevation moraines extending from the southern edge of the field are consistently among the lowest-transpiring sections of the field. These features also correspond with areas that had consistently lower measurements of LAI across measurement dates. This is consistent with previous findings of soil water availability and topography as strong drivers of year-end yield (Kravchenko and Bullock, 2000; Kumhálová et al., 2011), indicating that HRMET's high-resolution

Table 1
Water availability proxies.

Precipitation [mm]	June 22	July 30	August 29
Previous 2 weeks	6.4	101.1	47.0
Mean soil moisture [m^3 m^{-3}]	June 22	July 30	August 29
W-1	0.109	0.172	0.187
W-4	0.039	0.114	0.154
W-5	0.142	0.170	0.211
W-6	0.030	0.101	0.081
W-7	0.115	0.132	0.165
W-8	0.136	0.208	0.262

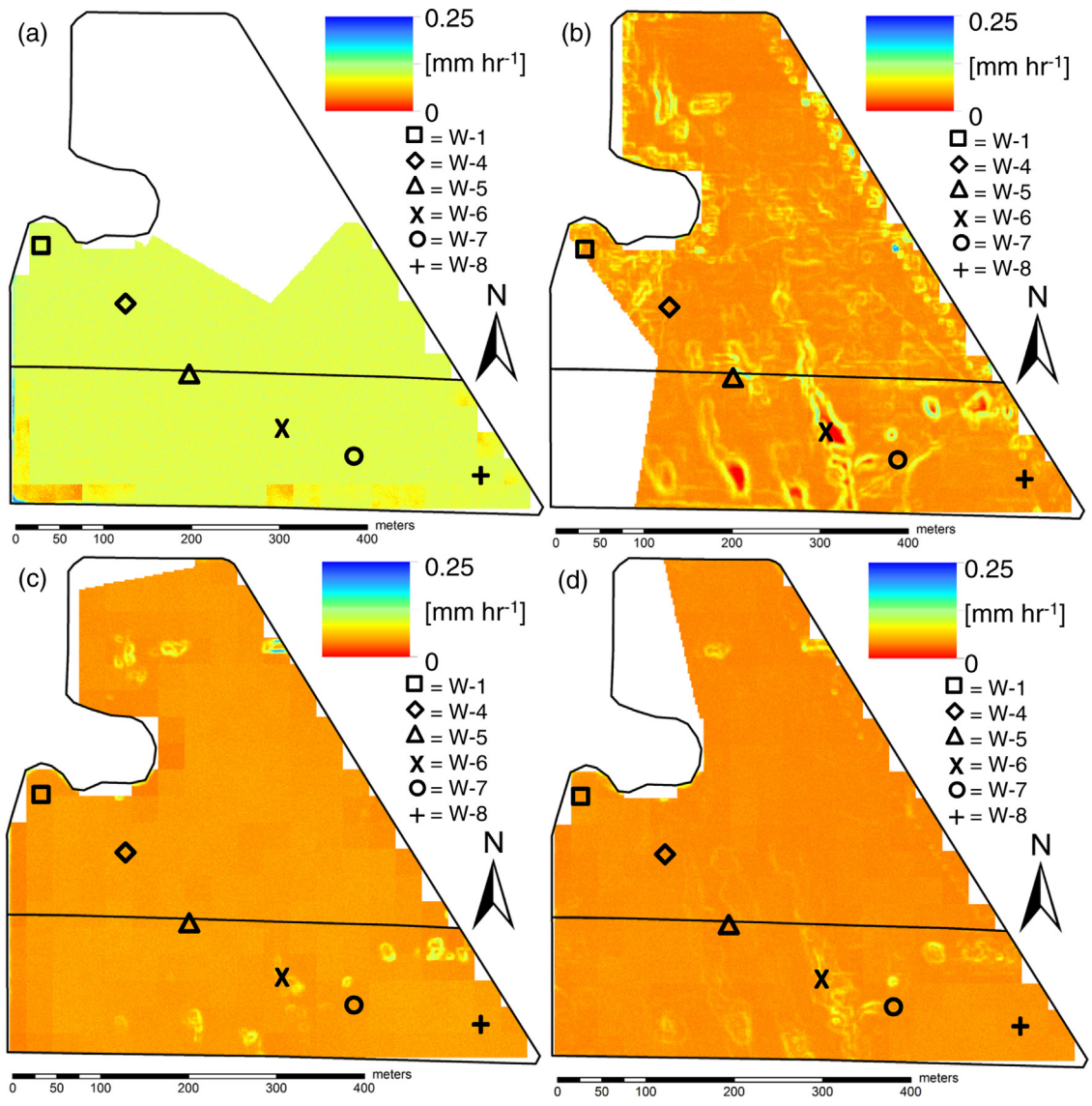

Fig. 7. Standard deviation of HRMET-calculated ET rates for (a) May 25, (b) June 22, (c) July 30, and (d) August 29 in mm h^{-1}. All images stretched linearly to the same range. Regions of highest variability tend to be those surrounding 'hot spots' in the thermal imagery, which correspond to regions of very low ET rates in Fig. 6.

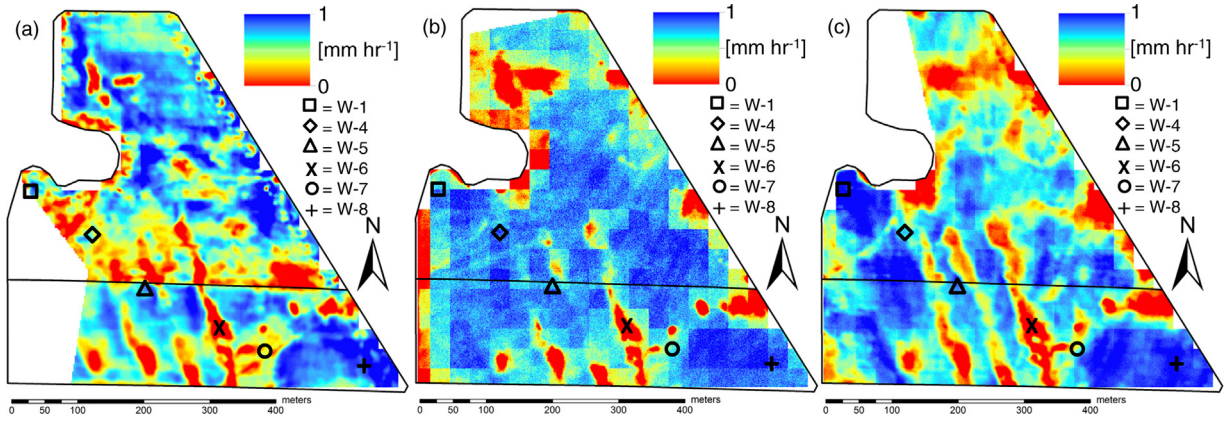

Fig. 8. ET_R over the fields using HRMET for (a) June 22, (b) July 30, and (c) August 29, normalized to the 5th & 95th percentile of ET rates within each field. Persistent patterns are apparent across measurement dates.

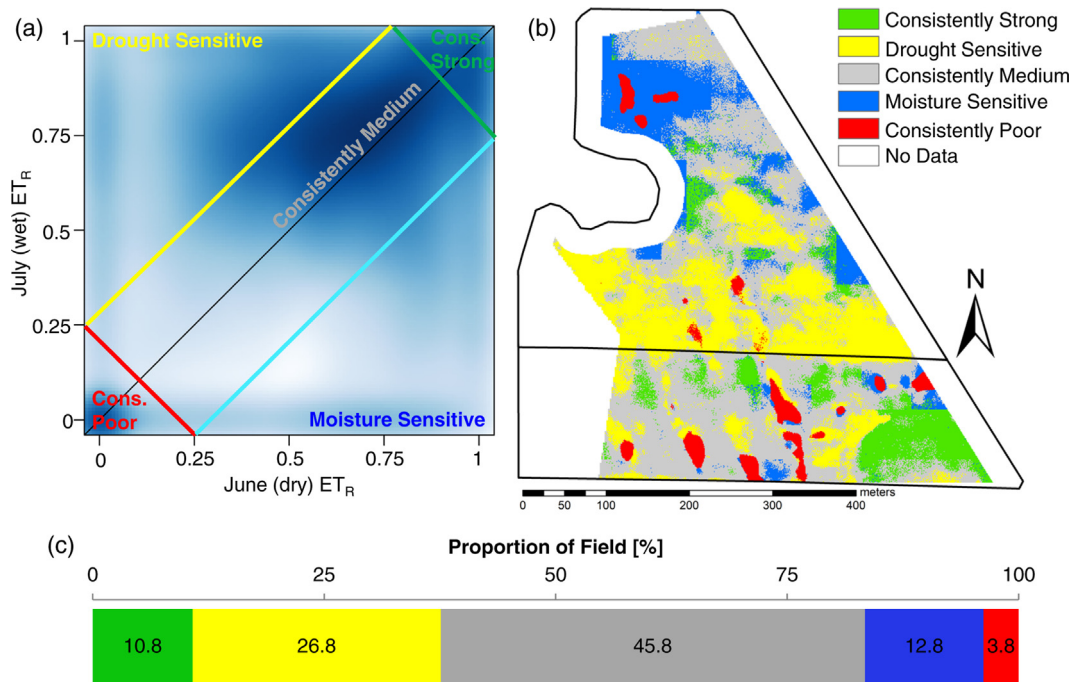

Fig. 9. Using ET_R (see Fig. 8) as a tool for mapping meter-scale sensitivity to moisture and drought stress. (a) shows a pixel-by-pixel comparison between ET_R rates in June (drought conditions) and July (rainfall in preceding week). Darker regions of the scatterplot correspond to greater densities of pixels. These are then mapped on the field-scale in (b) to demonstrate spatial patterns and the percentage of the field in each class is shown in (c).

ET maps can capture these patterns in a non-destructive and remote manner at high spatial resolution within the growing season.

Identification of these persistent patterns using ET_R is a valuable application of HRMET. Temporal delays from image acquisition to user availability present a major obstacle to the use of remote sensing data in precision agriculture; Anderson et al. (2004) noted that, for irrigation scheduling or variable-rate nutrient application, farmers must have information about crop health in near-real-time. ET_R rates provide a useful tool for identifying stressed regions on a subfield scale; the persistence of these patterns between dates means that a single image can be used to help guide future management decisions and identify sensitive regions even when very low stress levels exist, and indicates that ET patterns on a subfield scale are driven by fairly static factors.

4.5. Mapping drought sensitivity

As noted above, persistent patterns in ET across the field appear to be driven by fairly static factors such as soil texture and water availability. Any deviations from these patterns, therefore, indicate a spatially non-uniform response to external forcings. Fig. 9 presents a novel paired-image technique allowing us to explore differences in ET_R between dates using a comparison between our wet image (July) and our dry image (June). This allows us to identify sensitivity to different stressors on a subfield scale. To avoid potential edge effects observed in Figs. 6–8 due to large Landsat pixel size, we did not analyze sensitivity on the 30 m closest to roadways or buildings on the east and west borders of the field. Our paired-image technique is based on the principles of binary-image change detection, which is common in the remote sensing community (Singh, 1989; Lu et al., 2004). Change detection, typically using multispectral data from an earth-orbiting satellite such as Landsat, is often applied to agriculture to study land use and management practices such as cropping intensity (Jain et al., 2013), harvest monitoring (El Hajj et al., 2009), crop type distributions (Zhong et al., 2011), or crop rotations (Martinez-Casasnovas et al., 2005). However, applying change detection techniques to modeled data on a subfield scale is less common. Our paired-image method is, in essence, a within-season change vector analysis (CVA) technique that uses normalized ET_R data to divide a field into 5 distinct classes. This facilitates the visualization of the change vectors and image interpretation by the end-user (Fig. 9b). Using multiple dry or wet images and more advanced change detection algorithms may improve the efficacy and consistency of these sensitivity class maps (Ozdogan et al., 2010).

It is important to note that, by comparing ET_R rather than ET rates here, we are able to eliminate between-date variability in ET rates that could be driven by confounding factors such as meteorological conditions or development stage. Fig. 9a shows scatterplot of ET_R at each pixel, comparing our wet and dry images. A 1:1 relationship would mean that the field had the exact same spatial distribution of ET_R in both images and the map of ET_R would look identical between dates, though the magnitude of absolute ET rates could differ between dates. In other words, each pixel within the field would be transpiring at the same level relative to the rest of the field across both measurement dates.

Based on this relationship, Fig. 9a is divided into 5 categories corresponsing to different responses to changing water availability, which are mapped in Fig. 9b. Fig. 9c shows the proportion of each of these classes. Consistently high, consistently medium, and consistently low regions of the field are those that perform at approximately the same relative level between dates. These areas include the coarse-textured, high-topography regions identified earlier (consistently low) as well as a low-lying depression in the southeastern corner of the field (consistently high). Consistently medium areas are generally at intermediate terrain. These sensitivity classes provide a metric to evaluate the persistence of pattern noted in Section 4.4, and the majority of the field (70%) is classified as consistent (high, medium, and low) across both dates.

By comparing a wet and dry image, we can also map the sensitivity to drought stress on a subfield scale. Pixels identified as drought sensitive perform worse, relative to the rest of the field, during the dry image, indicating that they are responding to changes in water availability before the rest of the field. The majority of the inconsistent regions are identified as drought sensitive (27% of field). Conversely, moisture-sensitive regions (13% of field) perform worse, relative to the rest of the field, during the wet image. This disparity between drought-sensitivity and moisture-sensitivity is driven by the prevailing growing season weather conditions–the study site region experienced severe drought during the 2012 growing seasons, leaving crops vulnerable to water stress.

One of the major obstacles preventing land managers from incorporating remote sensing into agriculture is the turnaround time from image acquisition to information availability – while processing can often take days to weeks, decision-makers need information on the order of hours to days (Moran et al., 1997; Seelan et al., 2003; Mulla, 2013). Maps of sensitivity class provide a valuable subsititute for real-time information about crop health, which is not always available. A sensitivity map generated during a short dry period could be used to guide management during a future drought. This knowledge can then be used to improve forecast-based irrigation or nutrient application (e.g. Raghuwanshi and Wallender, 1999; Cai et al., 2011) and alleviate stress before significant yield impacts are felt.

5. Conclusions

We have developed a field-validated model, High Resolution Mapping of EvapoTranspiration (HRMET), that uses a combination of biophysical principles and established empirical relationships to calculate the land surface energy balance at high spatial resolution with easily-obtained data inputs. It takes advantage of an iterative approach to calculating the turbulent heat fluxes, and therefore does not require a hot and cool pixel like many other surface energy balance models (e.g. Menenti and Choudhury, 1993; Bastiaanssen et al., 1998; Allen et al., 2007) and is applicable over entire growing seasons at high resolutions.

We then demonstrate the utility of HRMET at two corn fields in south-central Wisconsin during the 2012 growing season. HRMET results (Fig. 6) suggest that the magnitude of subfield scale variability in ET rates is primarily driven by the availability of water. This has previously been demonstrated regarding year-end yield (Lark et al., 1998; Raghuwanshi and Wallender, 1997); however, there are practical limits to the spatial resolution at which yield mapping software can be employed (Lark et al., 1997). HRMET provides a rapid and non-destructive technique to identify subfield spatial and temporal variability in crop performance at multiple points within a single growing season.

We introduce relative ET (ET_R), a new technique for analyzing spatially distributed ET maps (Fig. 8). ET_R provides a simple normalization between dates that simultaneously translates ET to a more intuitive metric for land managers and highlights persistent patterns in the spatial distribution of ET rates. Patterns observed in ET_R appear to be driven primarily by slowly-changing factors such as soil water availability and topography, as has been documented in previous studies (Lark et al., 1998; Delin et al., 2000; Kravchenko and Bullock, 2002; Kravchenko et al., 2003; Kumhálová et al., 2011). Using ET_R, we present a novel paired-image technique for analyzing subfield sensitivity to stressors. A comparison of ET_R rates between wet and dry conditions reveals that 70% of our study site can be classified as fairly consistent between dates, 27% can be classified as drought-sensitive, and 13% can be classified as moisture sensitive (Fig. 9). Subfield sensitivity classification enables precision agriculture to use remotely sensed data in day-to-day management decisions.

Acknowledgments

The authors would like to thank the land owner who provided access to his fields. Phil Townsend provided helpful comments and suggestions throughout the project, and Ben Spaier assisted with image processing. Eric Booth, Melissa Motew, Jeff Oimoen and the Wisconsin Department of Natural Resources assisted with the thermal imagery acquisition. Eric Booth, Erin Gross, and Taylor Pomije assisted with field data collection. Chris Kucharik, Eric Booth, Evren Soylu, Carolyn Voter, and an anonymous reviewer provided helpful comments on an earlier draft of the manuscript. S.C.Z. and data collection efforts were supported by the National Science Foundation Water Sustainability & Climate Program (DEB-1038759), the North Temperate Lakes Long-Term Ecological Research Program (DEB-0822700) and the University of Wisconsin-Madison Anna Grant Birge Award.

References

Akhtar, F., Tischbein, B., Awan, U.K., 2013. Optimizing deficit irrigation scheduling under shallow groundwater conditions in lower reaches of Amu Darya River Basin. Water Resour. Manage. 27 (8), 3165–3178, http://dx.doi.org/10.1007/s11269-013-0341-0.

Alchanatis, V., Cohen, Y., Cohen, S., Moller, M., Sprinstin, M., Meron, M., Tsipris, J., Saranga, Y., Sela, E., 2010. Evaluation of different approaches for estimating and mapping crop water status in cotton with thermal imaging. Precis. Agric. 11 (1), 27–41, http://dx.doi.org/10.1007/s11119-009-9111-7.

Allen, R.G., Pereira, L.S., Raes, D., Smith, M., 1998. FAO Irrigation and Drainage Paper No. 56. United Nations, Rome, Italy, pp. 1–300.

Allen, R.G., Tasumi, M., Morse, A., Trezza, R., Wright, J.L., Bastiaanssen, W., Kramber, W., Lorite, I., Robison, C.W., 2007. Satellite-based energy balance for mapping evapotranspiration with internalized calibration (METRIC) –applications. J. Irrig. Drain. E. 133, 395–406.

Anderson, M.C., Allen, R.G., Morse, A., Kustas, W.P., 2012a. Use of Landsat thermal imagery in monitoring evapotranspiration and managing water resources. Remote Sens. Environ. 122, 50–65, http://dx.doi.org/10.1016/j.rse.2011.08.025.

Anderson, M.C., Neale, C.M.U., Li, F., Norman, J.M., Kustas, W.P., Jayanthi, H., Chavez, J., 2004. Upscaling ground observations of vegetation water content, canopy height, and leaf area index during SMEX02 using aircraft and Landsat imagery. Remote Sens. Environ. 92 (4), 447–464, http://dx.doi.org/10.1016/j.rse.2004.03.019.

Anderson, R.G., Lo, M.-H., Famiglietti, J.S., 2012b. Assessing surface water consumption using remotely-sensed groundwater, evapotranspiration, and precipitation. Geophys. Res. Lett. 3, 9, http://dx.doi.org/10.1029/2012GL052400.

Bastiaanssen, W.G.M., Cheema, M.J.M., Immerzeel, W.W., Miltenburg, I.J., Pelgrum, H., 2012. Surface energy balance and actual evapotranspiration of the transboundary Indus Basin estimated from satellite measurements and the ETLook model. Water Resour. Res. 48 (11), http://dx.doi.org/10.1029/2011WR010482.

Bastiaanssen, W.G.M., Menenti, M., Feddes, R.A., Holtslag, A.A.M., 1998. A remote sensing surface energy balance algorithm for land (SEBAL). 1. Formulation. J. Hydrol. 212–213, 198–212, http://dx.doi.org/10.1016/S0022-1694(98)00253-4.

Berni, J.A.J., Zarco-Tejada, P.J., Sepulcre-Canto, G., Fereres, E., Villalobos, F., 2009. Mapping canopy conductance and CWSI in olive orchards using high resolution thermal remote sensing imagery. Remote Sens. Environ. 113 (11), 2380–2388, http://dx.doi.org/10.1016/j.rse.2009.06.018.

Brisson, N., Itier, B., L'Hotel, J.C., Lorendeau, J.Y., 1998. Parameterisation of the Shuttleworth-Wallace model to estimate daily maximum transpiration for use in crop models. Ecol. Model. 107 (2), 159–169.

Cai, X., Hejazi, M.I., Wang, D., 2011. Value of probabilistic weather forecasts: Assessment by real-time optimization of irrigation scheduling. J. Water Resour. Pl.-ASCE 137 (5), 391–403, http://dx.doi.org/10.1061/(ASCE)WR.1943-5452.0000126.

Camillo, P., Gurney, R., 1986. A resistance parameter for bare-soil evaporation models. Soil Sci. 141 (2), 95–105, http://dx.doi.org/10.1097/00010694-198602000-00001.

Campbell, G. S., & Norman, J. M. (2000). An Introduction to Environmental Biophysics (2nd ed.). Springer.

Chavez, J.L., Gowda, P.H., Howell, T.A., Neale, C.M.U., Copeland, K.S., 2009. Estimating hourly crop ET using a two-source energy balance model and multispectral airborne imagery. Irrigation Sci. 28 (1), 79–91, http://dx.doi.org/10.1007/s00271-009-0177-9.

Chen, J.M., Cihlar, J., 1996. Retrieving leaf area index of boreal conifer forests using Landsat TM images. Remote Sens. Environ. 55, 153–162.

Cicek, H., Sunohara, M., Wilkes, G., McNairn, H., Pick, F., Topp, E., Lapen, D.R., 2010. Using vegetation indices from satellite remote sensing to assess corn and

soybean response to controlled tile drainage. Agric. Water Manage. 98 (2), 261–270, http://dx.doi.org/10.1016/j.agwat.2010.08.019.
Clayton, L., Attig, J.W., 1997. Pleistocene Geology of Dane County, Wisconsin. Wisconsin Geological and Natural History Survey, Madison WI.
Crawford, T.M., Duchon, C.E., 1999. An improved parameterization for estimating effective atmospheric emissivity for use in calculating daytime downwelling longwave radiation. J. Appl. Meteorol. 38 (4), 474–480.
Delin, G.N., Healy, R.W., Landon, M.K., Böhlke, J.K., 2000. Effects of topography and soil properties on recharge at two sites in an agricultural field. J. Am. Water Resour. Assoc. 36 (6), 1401–1416.
El Hajj, M., Begue, A., Guillaume, S., Martine, J.-F., 2009. Integrating SPOT-5 time series, crop growth modeling and expert knowledge for monitoring agricultural practices - The case of sugarcane harvest on Reunion Island. Remote Sens. Environ. 113 (10), 2052–2061, http://dx.doi.org/10.1016/j.rse.2009.04.009.
Elhaddad, A., Garcia, L.A., Chávez, J.L., 2010. Using a surface energy balance model to calculate spatially distributed actual evapotranspiration. J. Irrig. Drain. E. 137 (1), 17–26.
Er-Raki, S., Chehbouni, A., Guemouria, N., Duchemin, B., Ezzahar, J., Hadria, R., 2007. Combining FAO-56 model and ground-based remote sensing to estimate water consumptions of wheat crops in a semi-arid region. Agric. Water Manage. 87 (1), 41–54, http://dx.doi.org/10.1016/j.agwat.2006.02.004.
Farahani, H., Bausch, W., 1995. Performance of evapotranspiration models for maize - bare soil to closed canopy. T. ASAE 38 (4), 1049–1059.
Folhes, M.T., Renno, C.D., Soares, J.V., 2009. Remote sensing for irrigation water management in the semi-arid Northeast of Brazil. Agric. Water Manage. 96 (10), 1398–1408, http://dx.doi.org/10.1016/j.agwat.2009.04.021.
Glenn, E.P., Huete, A.R., Nagler, P.L., Hirschboeck, K.K., Brown, P., 2007. Integrating remote sensing and ground methods to estimate evapotranspiration. Crit. Rev. Plant Sci. 26 (3), 139–168, http://dx.doi.org/10.1080/07352680701402503.
Gonzalez-Dugo, M.P., Moran, M.S., Mateos, L., Bryant, R., 2006. Canopy temperature variability as an indicator of crop water stress severity. Irrigation Sci. 24 (4), 233–240, http://dx.doi.org/10.1007/s00271-005-0022-8.
Gowda, P.H., Chavez, J.L., Colaizzi, P.D., Evett, S.R., Howell, T.A., Tolk, J.A., 2007. ET mapping for agricultural water management: present status and challenges. Irrigation Sci. 26 (3), 223–237, http://dx.doi.org/10.1007/s00271-007-0088-6.
Hiler, E.A., Howell, T.A., Lewis, R.B., Boos, R.P., 1974. Irrigation timing by the stress day index method. T. ASAE 17 (3), 393–398.
Huang, X., Wang, L., Yang, L., Kravchenko, A.N., 2008. Management effects on relationships of crop yields with topography represented by wetness index and precipitation. Agron. J. 100 (5), 1463, http://dx.doi.org/10.2134/agronj2007.0325.
Hunsaker, D.J., Barnes, E.M., Clarke, T.R., Fitzgerald, G.J., Pinter Jr., P.J., 2005. Cotton irrigation scheduling using remotely sensed and FAO-56 basal crop coefficients. T. ASAE 48 (4), 1395–1407.
Idso, S.D., Jackson, R.D., Reginato, R.J., 1977. Remote-sensing of crop yields. Science 196 (4285), 19–25, http://dx.doi.org/10.1126/science.196.4285.19.
Jackson, R.D., Idso, S.B., Reginato, R.J., Pinter, P.J., 1981. Canopy temperature as a crop water-stress indicator. Water Resour. Res. 17 (4), 1133–1138, http://dx.doi.org/10.1029/WR017i004p01133.
Jain, M., Mondal, P., DeFries, R.S., Small, C., Galford, G.L., 2013. Mapping cropping intensity of smallholder farms: a comparison of methods using multiple sensors. Remote Sens. Environ. 134, 210–223, http://dx.doi.org/10.1016/j.rse.2013.02.029.
Jury, W.A., Horton, R., 2004. Soil Physics, (6th ed.). J. Wiley., Hoboken, NJ.
Kanwar, R.S., Johnson, H.P., Fenton, T.E., 1984. Determination of crop production loss due to inadequate drainage in a large watershed. J. Am. Water Resour. Assoc. 20 (4), 589–597.
King, B.A., Kincaid, D.C., 2004. A variable flow rate sprinkler for site-specific irrigation management. Appl. Eng. Agric. 20 (6), 765–770.
Ko, J., Piccinni, G., 2009. Corn yield responses under crop evapotranspiration-based irrigation management. Agric. Water Manage. 96 (5), 799–808, http://dx.doi.org/10.1016/j.agwat.2008.10.010.
Kondo, J., Saigusa, N., Sato, T., 1990. A parameterization of Evaporation from bare soil surfaces. J. Appl. Meteorol. 29 (5), 385–389, http://dx.doi.org/10.1175/1520-0450(1990)029<0385:APOEFB>2.0.CO;2.
Kravchenko, A.N., Bullock, D.G., 2000. Correlation of corn and soybean grain yield with topography and soil properties. Agron. J. 92 (1), 75–83, http://dx.doi.org/10.1007/s100870050010.
Kravchenko, A.N., Bullock, D.G., 2002. Spatial variability of soybean quality data as a function of field topography: II. A proposed technique for calculating the size of the area for differential soybean harvest. Crop Sci. 42 (3), 816–821.
Kravchenko, A.N., Thelen, K.D., Bullock, D.G., Miller, N.R., 2003. Relationship among crop grain yield, topography, and soil electrical conductivity studied with cross-correlograms. Agron. J. 95 (5), 1132–1139.
Kresovic, B., Dragicevic, V., Gajic, B., Tapanarova, A., Pejic, B., 2013. The dependence of maize (Zea mays) hybrids yielding potential on the water amounts reaching the soil surface. Genetika 45 (1), 261–272, http://dx.doi.org/10.2298/GENSR1301261K.
Kucharik, C.J., Brye, K.R., 2003. Integrated Biosphere Simulator (IBIS) yield and nitrate loss predictions for Wisconsin maize receiving varied amounts of nitrogen fertilizer. J. Environ. Qual. 32 (1), 247–268.
Kucharik, C.J., Twine, T.E., 2007. Residue, respiration, and residuals: Evaluation of a dynamic agroecosystem model using eddy flux measurements and biometric data. Agric. Forest Meteorol. 146 (3-4), 134–158, http://dx.doi.org/10.1016/j.agrformet.2007.05.011.
Kumhálová, J., Kumhála, F., Kroulík, M., Matějková, Š., 2011. The impact of topography on soil properties and yield and the effects of weather conditions. Precision Agric. 12 (6), 813–830, http://dx.doi.org/10.1007/s11119-011-9221-x.
Lark, R.M., Catt, J.A., Stafford, J.V., 1998. Towards the explanation of within-field variability of yield of winter barley: soil series differences. J. Agric. Sci. 131 (4), 409–416.
Lark, R.M., Stafford, J.V., Bolam, H.C., 1997. Limitations on the spatial resolution of yield mapping for combinable crops. J. Agric. Eng. Res. 66 (3), 183–193, http://dx.doi.org/10.1006/jaer.1996.0132.
Loheide II, S.P., Gorelick, S.M., 2005. A local-scale, high-resolution evapotranspiration mapping algorithm (ETMA) with hydroecological applications at riparian meadow restoration sites. Remote Sens. Environ. 98 (2–3), 182–200, http://dx.doi.org/10.1016/j.rse.2005.07.003.
Lu, D., Mausel, P., Brondizio, E., Moran, E., 2004. Change detection techniques. Int. J. Remote Sens. 25 (12), 2365–2407, http://dx.doi.org/10.1080/0143116031000139863.
Maes, W.H., Steppe, K., 2012. Estimating evapotranspiration and drought stress with ground-based thermal remote sensing in agriculture: a review. J. Exp. Bot. 63 (13), 4671–4712, http://dx.doi.org/10.1093/jxb/err313.
Martinez-Casasnovas, J.A., Martin-Montero, A., Casterad, M.A., 2005. Mapping multi-year cropping patterns in small irrigation districts from time-series analysis of Landsat TM images. Eur. J. Agron. 23 (2), 159–169, http://dx.doi.org/10.1016/j.eja.2004.11.004.
Masek, J. G., Vermote, E. F., Saleous, N., Wolfe, R., Hall, F. G., Huemmrich, F., Gao, F., Kutler, J., & Lim, T. K. (2006). LEDAPS Landsat Calibration, Reflectance, Atmospheric Correction Preprocessing Code. Oak Ridge, Tennessee: Oak Ridge National Laboratory Distributed Active Archive Center. Retrieved from http://dx.doi.org/10.3334/ORNLDAAC/1080
Menenti, M., Choudhury, B.J., 1993. Parameterization of land surface evaporation by means of location dependent potential evaporation and surface temperature range. Exchange Processes at the Land Surface for a Range of Space and Time Scales 212, 561–568.
Monteith, J.L., 1965. Evaporation and environment. Sym. Soc. Exp. Biol. 19, 205–234.
Moran, M.S., Clarke, T.R., Inoue, Y., Vidal, A., 1994. Estimating crop water deficit using the relation between surface-air temperature and spectral vegetation index. Remote Sens. Environ. 49 (3), 246–263, http://dx.doi.org/10.1016/0034-4257(94)90020-5.
Moran, M.S., Inoue, Y., Barnes, E.M., 1997. Opportunities and limitations for image-based remote sensing in precision crop management. Remote Sens. Environ. 61 (3), 319–346, http://dx.doi.org/10.1016/S0034-4257(97)00045-X.
Mulla, D.J., 2013. Twenty five years of remote sensing in precision agriculture: Key advances and remaining knowledge gaps. Biosys. Eng. 114 (4), 358–371, http://dx.doi.org/10.1016/j.biosystemseng.2012.08.009.
Norman, J.M., Kustas, W., Humes, K., 1995. Source approach for estimating soil and vegetation energy fluxes in observations of directional radiometric surface temperature. Agric. Forest Meteorol. 77 (3-4), 263–293, http://dx.doi.org/10.1016/0168-1923(95)02265-Y.
Norman, J.M., Becker, F., 1995. Terminology in thermal infrared remote sensing of natural surfaces. Agric. Forest Meteorol. 77 (3-4), 153–166, http://dx.doi.org/10.1016/0168-1923(95)02259-Z.
Ozdogan, M., Yang, Y., Allez, G., Cervantes, C., 2010. Remote sensing of irrigated agriculture: opportunities and challenges. Remote Sens. 2 (9), 2274–2304, http://dx.doi.org/10.3390/rs2092274.
Raghuwanshi, N.S., Wallender, W.W., 1997. Field-measured evapotranspiration as a stochastic process. Agric. Water Manage. 32 (2), 111–129.
Raghuwanshi, N.S., Wallender, W.W., 1999. Forecasting and optimizing furrow irrigation management decision variables. Irrigation Sci. 19 (1), 1–6, http://dx.doi.org/10.1007/s002710050065.
Raupach, M.R., 1994. Simplified expressions for vegetation roughness length an zero-plane displacement as functions of canopy height an area index. Boundary-Layer Meteorology 71 (1-2), 211–216.
Roerink, G.J., Su, Z., Menenti, M., 2000. S-SEBI: a simple remote sensing algorithm to estimate the surface energy balance. Phys. Chem. Earth B 25 (2), 147–157, http://dx.doi.org/10.1016/S1464-1909(99)00128-8.
Schepers, A.R., Shanahan, J.F., Liebig, M.A., Schepers, J.S., Johnson, S.H., Luchiari, A., 2004. Appropriateness of management zones for characterizing spatial variability of soil properties and irrigated corn yields across years. Agron. J. 96 (1), 195–203.
Schmidt, J.P., DeJoia, A.J., Ferguson, R.B., Taylor, R.K., Young, R.K., Havlin, J.L., 2002. Corn yield response to nitrogen at multiple in-field locations. Agron. J. 94 (4), 798–806.
Seela, S.K., Laguette, S., Casady, G.M., Seielstad, G.A., 2003. Remote sensing applications for precision agriculture: A learning community approach. Remote Sens. Environ. 88 (1–2), 157–169, http://dx.doi.org/10.1016/j.rse.2003.04.007.
Serbin, S.P., Singh, A., McNeil, B.E., Kingdon, C.C., Townsend, P.A., 2014. Spectroscopic determination of leaf morphological and biochemical traits for northern temperate and boreal tree species. Ecol. Appl., http://dx.doi.org/10.1990/13-2110.1.
Shahabfar, A., Eitzinger, J., 2011. Agricultural drought monitoring in semi-arid and arid areas using MODIS data. J. Agric. Sci. 149, 403–414, http://dx.doi.org/10.1017/S0021859610001309.
Shuttleworth, W.J., Wallace, J.S., 1985. Evaporation from sparse crops-an energy combination theory. Q. J. Roy. Meteorol. Soc. 111 (469), 839–855.
Singh, A., 1989. Digital change detection techniques using remotely-sensed data. Int. J. Remote Sens. 10 (6), 989–1003.
Soylu, M.E., Kucharik, C.J., Loheide II, S.P., 2014. Development of an integrated agroecosystem-variably saturated soil water flow model

to evaluate the influence of groundwater on plant physiology and energy balance. Agric. Forest Meteorol. 189–190 (1–2), 198–210, http://dx.doi.org/10.1016/j.agrformet.2014.01.019.

Suleiman, A., Crago, R., 2004. Hourly and daytime evapotranspiration from grassland using radiometric surface temperatures. Agron. J. 96 (2), 384–390.

Welles, J.M., Norman, J.M., 1991. Instrument for indirect measurement of canopy architecture. Agron. J. 83 (5), 818–825.

Wibawa, W.D., Dludlu, D.L., Swenson, L.J., Hopkins, D.G., Dahnke, W.C., 1993. Variable fertilizer application based on yield goal, soil fertility, and soil map unit. J. Prod. Agric. 6 (2), 255–261, http://dx.doi.org/10.2134/jpa1993.0255.

Wu, J., Zhou, L., Liu, M., Zhang, J., Leng, S., Diao, C., 2013. Establishing and assessing the Integrated Surface Drought Index (ISDI) for agricultural drought monitoring in mid-eastern China. Int. J. Appl. Earth Obs. 23, 397–410, http://dx.doi.org/10.1016/j.jag.2012.11.003.

Zheng, G., Moskal, L.M., 2009. Retrieving leaf area index (LAI) using remote sensing: theories, methods and sensors. Sensors 9 (4), 2719–2745, http://dx.doi.org/10.3390/s90402719.

Zhong, L., Hawkins, T., Biging, G., Gong, P., 2011. A phenology-based approach to map crop types in the San Joaquin Valley, California. Int. J. Remote Sens. 32 (22), 7777–7804, http://dx.doi.org/10.1080/01431161.2010.527397.

Zhou, M.C., Ishidaira, H., Hapuarachchi, H.P., Magome, J., Kiem, A.S., Takeuchi, K., 2006. Estimating potential evapotranspiration using Shuttleworth–Wallace model and NOAA-AVHRR NDVI data to feed a distributed hydrological model over the Mekong River basin. J. Hydrol. 327 (1–2), 151–173, http://dx.doi.org/10.1016/j.jhydrol.2005.11.013.